Progress In Electromagnetics Research C, Vol. 172, 350–359, 2026

PIER C

(Received 5 June 2026, Accepted 19 July 2026, Scheduled 17 August 2026)

Spaceborne MIMO SAR Maneuvering Target Imaging Based on Joint Radial Acceleration Estimation and Signal Reconstruction

Yingjia Li* and Kunyu Gao

College of Information Science and Engineering, Hohai University, Changzhou, China

ABSTRACT: In spaceborne multi-input multi-output synthetic aperture radar (MIMO SAR) ground moving target indication (GMTI), the unknown radial acceleration of a target induces severe Doppler spectral broadening, while mismatched conventional reconstruction filters lead to significant image defocusing. To address these challenges, this paper proposes a novel focused imaging method that seamlessly integrates radial acceleration estimation with reconstruction filter design. This method first adaptively suppresses static background clutter by utilizing the extended multi-channel clutter suppression interferometer (M-CSI) technique. On this basis, the frequency-domain cross-correlation characteristics of time-domain sub-aperture signals recovered via inverse reconstruction filtering are exploited to estimate the target radial acceleration deeply buried in residual clutter. Furthermore, a ratio factor resistant to amplitude interference is constructed to search for the radial velocity. Finally, a reconstruction filter for maneuvering targets is designed using the obtained motion parameters, completing the unambiguous recovery of the original Doppler spectrum and pulse-compression focusing. Simulation results demonstrate that the proposed method can estimate the target maneuvering parameters, thereby thoroughly resolving the defocusing and artifact issues.

1. INTRODUCTION

Spaceborne synthetic aperture radar (SAR) has all-weather, day-and-night, robust imaging capabilities, and plays an irreplaceable role in Earth observation [1]. With the ever-increasing demand for Earth observation, traditional single-channel SAR systems face an inherent bottleneck of a contradiction between high spatial resolution and wide swath (HRWS). To address this issue, multi-channel architectures have been widely introduced. By configuring multiple receiving sub-apertures in the azimuth direction and employing a relatively low pulse repetition frequency (PRF), the unambiguous swath coverage is effectively expanded [2–4]. In recent years, multiple-input multiple-output (MIMO) SAR technology has further extended the system's spatial degrees of freedom by transmitting multiple orthogonal waveforms. This not only significantly enhances HRWS imaging performance but also provides a superior physical foundation for ground moving target indication (GMTI) and clutter suppression techniques [5–7].

In spaceborne MIMO SAR systems, the echo signals of ground maneuvering targets are usually deeply buried in strong surface clutter. Moreover, influenced by the target's kinematic state, its Doppler spectrum suffers from complex distortions. Traditional clutter suppression techniques, such as the displaced phase center antenna (DPCA) [8] and space-time adaptive processing (STAP) [9, 10], often face stringent constraints regarding system array conditions or massive computational complexity, presenting numerous limitations in practical engineering applications. As an effective alternative, the multi-channel clutter suppression interferometer (M-CSI) has been applied to clutter suppression tasks in spatial multi-channel SAR because it avoids the estimation of high-dimensional covariance matrices. However, due to azimuth Doppler spectrum aliasing caused by low PRF of spaceborne systems, a reconstruction filter for stationary targets must first be used to perform unambiguous spectrum reconstruction on the azimuth-undersampled data before the M-CSI algorithm can be effectively applied to interferometric cancellation.

It is worth noting that existing M-CSI-based parameter estimation and imaging methods, such as those in [11], are established under the ideal assumption of a target undergoing uniform linear motion primarily focusing on extraction and compensation of radial velocity. However, in practical observation scenarios, a non-cooperative ground maneuvering target inevitably exhibits complex maneuvering behaviors. The presence of the target's radial acceleration directly alters the azimuth Doppler rate of the echo signal, leading to severe spectral broadening and distortion in the azimuth direction. This causes the target to suffer from severe azimuth defocusing, energy dispersion, and even artifacts in the final SAR image. To achieve well-focused, artifact-free imaging of maneuvering targets, it is necessary to design a reconstruction filter for maneuvering targets under nonuniform sampling conditions. However, the design of such a filter necessitates prior knowledge of the target's motion parameters, specifically its radial acceleration and radial velocity. To accurately estimate the motion parameters of the maneuvering target, advanced long-time coherent inte-

* Corresponding author: Yingjia Li (lyj1686529682@163.com).

gration algorithms, such as generalized Radon–Fourier transform (GRFT) [12, 13], have been proposed. Although GRFT can jointly estimate velocity and acceleration by compensating for range curvature and Doppler frequency migration, its reliance on a multi-dimensional traversal search incurs a prohibitive computational burden, severely limiting its practical efficiency. Recently, a cascaded framework [14] designed for airborne platforms employs a clutter-suppression strategy similar to M-CSI; nevertheless, its acceleration-estimation step still inherently relies on a search-based strategy.

To address the inadequate consideration of target acceleration characteristics in existing studies, this paper extends the conventional ground target motion model to encompass complex maneuvering scenarios. Furthermore, this paper proposes a highly efficient, search-free radial acceleration estimation algorithm and a novel reconstruction filter for maneuvering targets tailored specifically for undersampled and non-uniformly sampled spaceborne MIMO SAR systems. Specifically, based on establishing two-way slant-range and multi-channel signal-echo models for maneuvering target, this paper first systematically derives a reconstruction filter for maneuvering targets applicable to complex maneuvering scenarios. In the signal preprocessing stage, an extended M-CSI algorithm is used to effectively filter out stationary environmental clutter while preserving the effective energy of maneuvering target. To resolve the destruction of the original spectral characteristics of the maneuvering target caused by the interferometric phase, this paper recovers observation signals of each channel via an inverse reconstruction filter for stationary targets and proposes to divide the complete synthetic aperture time into early and late sub-apertures. By utilizing the frequency-domain cross-correlation delay of the sub-aperture signals, the radial acceleration of the target is precisely inverted and solved. Based on the obtained acceleration estimation, a ratio factor independent of the channel signal amplitude is constructed, enabling an accurate estimation of the maneuvering target's radial velocity via a traversal search. Finally, using the complete set of acquired maneuvering parameters, a reconstruction filter for maneuvering targets is designed to achieve high-quality pulse-compression focused imaging.

2. MANEUVERING TARGET SIGNAL MODEL

Assume that the geometric configuration of the spaceborne MIMO SAR system observing a ground maneuvering target is illustrated in Fig. 1. The radar platform undergoes level flight at a constant velocity v along the y-axis (azimuth direction). The antenna array is configured with N_e and N_a receiving subapertures in elevation and azimuth directions, respectively. On the transmitter side, two azimuth antennas (denoted as $Tx1$ and $Tx2$, corresponding to the red and blue indicators in the figure, respectively) synchronously transmit short-time shift orthogonal (STSO) waveform 1 and waveform 2 [5]. The motion state of the maneuvering target P within the scene can be decomposed into a radial motion component (comprising the radial velocity v_r and radial acceleration a_r) and an along-track motion component (comprising the along-track velocity v_y and along-track acceleration a_y). Given that the operational veloc-

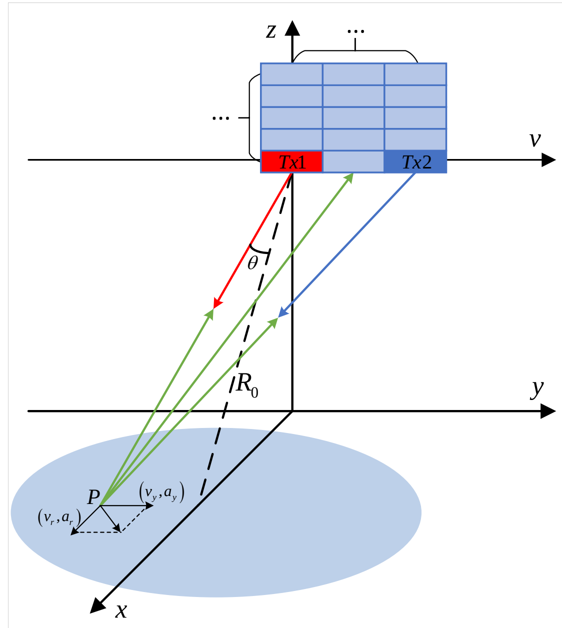

FIGURE 1. Geometric configuration of the spaceborne MIMO SAR system.

ity of the spaceborne platform is substantially higher than the along-track velocity of typical ground targets, the relative impact of the along-track motion component on signal modulation is extremely small; hence, it is neglected in the subsequent theoretical derivations. Meanwhile, it is reasonably assumed that the radial motion parameters of the target remain constant in a complete synthetic aperture time.

To exploit enhanced spatial degrees of freedom in the azimuth direction, the receiver of a MIMO-SAR system must reliably separate the mixed short-term shift-orthogonal (STSO) waveforms. The specific separation scheme is determined by the transmission time delay between the two waveforms. When the delay is less than half of the pulse duration, the waveforms preserve strong time-domain orthogonality and can be efficiently extracted using time-domain filtering. However, if the delay exceeds this threshold and time-domain orthogonality is compromised, the digital beamforming (DBF) technique applied to the elevation receiving array becomes essential to guaranteeing lossless waveform separation in the spatial domain [5]. To highlight the core algorithmic mechanism, the subsequent theoretical analysis in this paper is established on the assumption that the waveforms have been completely separated, focusing primarily on the azimuth Doppler modulation characteristics of the echo signals.

Based on the aforementioned geometric topology, the scattering echo paths of the maneuvering target for the two STSO waveforms exhibit spatial differences. Specifically, the instantaneous two-way slant range histories experienced by waveform 1 and waveform 2 can be precisely modeled, respectively, as:

$$\begin{aligned} R_1(t_m) = & \sqrt{(R_0+v_r t_m+0.5a_r t_m^2)^2+(v t_m)^2} \\ & +\sqrt{(R_0+v_r t_m+0.5a_r t_m^2)^2+(v t_m+\Delta x_{n_a})^2} \end{aligned} \tag{1}$$

$$R_2(t_m) = \sqrt{(R_0+v_r t_m+0.5a_r t_m^2)^2+(v t_m+(N_a-1)d_a)^2}$$

$$+\sqrt{(R_0+v_rt_m+0.5a_rt_m^2)^2+(vt_m+\Delta x_{n_a})^2} \quad (2)$$

where R_0 is the closest slant range; t_m is the slow time; $\Delta x_{n_a} = (n_a - 1)d_a$ denotes the distance between the n_ath receiving sub-channel and $Tx1$ in the azimuth direction; and d_a is the azimuth sub-channel spacing.

Furthermore, constrained by the requirement for wide-swath observation, spaceborne MIMO SAR systems typically employ a low PRF. This azimuth undersampling scheme inevitably leads to severe aliasing in the Doppler spectra acquired by each receiving sub-channel, thereby significantly restricting the effective execution of subsequent target detection and imaging algorithms. Consequently, achieving precise and unambiguous reconstruction of the Doppler spectrum is an indispensable core procedure in the entire signal preprocessing pipeline. To address this issue, existing studies, such as [11] and [15], have respectively presented the design schemes of the reconstruction filter for stationary targets in ideal static scenes and the reconstruction filter for moving targets undergoing conventional uniform linear motion. To overcome limitations of the aforementioned models when dealing with complex maneuvering targets, the following section will derive, in detail, the reconstruction filter for maneuvering targets.

Applying the Taylor expansion to the two-way slant range of waveform 1 yields:

$$R_1(t_m)\approx 2R_0+\frac{\Delta x_{n_a}^2}{2R_0}+\frac{2v_rR_0+v\Delta x_{n_a}}{R_0}t_m+\frac{a_rR_0+v^2}{R_0}t_m^2 \quad (3)$$

Rearranging the above equation yields:

$$\begin{aligned} R_1(t_m) &= 2R_0+\frac{\Delta x_{n_a}^2}{4R_0}+2v_rt_m+a_rt_m^2+\frac{v^2}{R_0}\left(t_m+\frac{\Delta x_{n_a}}{2v}\right)^2 \\ &= 2R_0+\frac{\Delta x_{n_a}^2(2a-v^2)}{4aR_0}+2v_rt_m+\frac{a}{R_0}\left(t_m+\frac{v\Delta x_{n_a}}{2a}\right)^2 \end{aligned} \quad (4)$$

where $a = a_rR_0 + v^2$.

The baseband azimuth echo signal is mainly determined by the two-way slant-range history. Neglecting the amplitude envelope, the generic analytical model of the received signal can be written as:

$$s_{Tx1,n_a}(t_m) = \exp\left(\frac{-j2\pi R_1(t_m)}{\lambda}\right) \quad (5)$$

where λ is the wavelength of the carrier signal.

Therefore, the maneuvering target echo of waveform 1 received by the n_ath receiving sub-channel in the azimuth direction can be expressed as:

$$\begin{aligned} s_{Tx1,n_a}(t_m) = &\exp\left(\frac{-j4\pi R_0}{\lambda}\right)\exp\left(\frac{-j4\pi v_rt_m}{\lambda}\right) \\ &\exp\left(\frac{j\pi\Delta x_{n_a}^2(v^2-2a)}{2a\lambda R_0}\right) \\ &\exp\left(\frac{-j2\pi a}{\lambda R_0}\left(t_m+\frac{v\Delta x_{n_a}}{2a}\right)^2\right) \end{aligned} \quad (6)$$

Similarly, the maneuvering target echo of waveform 2 received by the n_ath receiving sub-channel in the azimuth direction can be expressed as:

$$\begin{aligned} s_{Tx2,n_a}(t_m) = &\exp\left(\frac{-j4\pi R_0}{\lambda}\right)\exp\left(\frac{-j4\pi v_rt_m}{\lambda}\right) \\ &\exp\left(\frac{j\pi(\Delta x_{n_a}+\Delta x_{N_a})^2(v^2-2a)}{2a\lambda R_0}\right) \\ &\exp\left(\frac{-j2\pi a}{\lambda R_0}\left(t_m+\frac{v(\Delta x_{n_a}+\Delta x_{N_a})}{2a}\right)^2\right) \end{aligned} \quad (7)$$

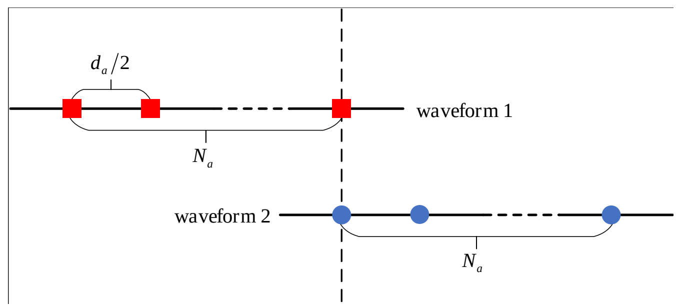

FIGURE 2. Schematic diagram of the effective phase center distribution.

As clearly depicted in Fig. 2, the spacing between adjacent equivalent phase centers is $d_a/2$, consistent with the theoretical derivation in (6) and (7). While waveform 1 and waveform 2 each provide N_a phase centers, one phase center coincides, resulting in a total of $2N_a-1$ unique equivalent phase centers for the system. Letting $M = 2N_a - 1$, the maneuvering target signal received by the mth ($1 \leqslant m \leqslant M$) equivalent receiving channel can be expressed as:

$$\begin{aligned} h_m(t_m) = &\exp\left(\frac{-j4\pi R_0}{\lambda}\right)\exp\left(\frac{j\pi\Delta x_m^2(v^2-2a)}{2a\lambda R_0}\right) \\ &\exp\left(\frac{-j4\pi v_rt_m}{\lambda}\right)\exp\left(\frac{-j2\pi a}{\lambda R_0}\left(t_m+\frac{v\Delta x_m}{2a}\right)^2\right) \end{aligned} \quad (8)$$

where $\Delta x_m = (m - 1)d_a$.

Meanwhile, the stationary target echo of the traditional single-channel SAR can be expressed as:

$$\bar{h}(t_m) = \exp\left(\frac{-j4\pi R_0}{\lambda}\right)\exp\left(\frac{-j2\pi v^2}{\lambda R_0}t_m^2\right) \quad (9)$$

By comparing (8) and (9), the maneuvering target echo signal of the MIMO SAR system couples four additional modulation components compared to the stationary target echo signal of the traditional single-channel SAR: 1) a constant phase, 2) a time-varying phase history dependent on the radial velocity, 3) a scaling factor that induces broadening or compression of the Doppler bandwidth, and 4) a time delay parameter corresponding to the spatial path difference.

Transforming (8) into the Doppler domain yields:

$$H_m(f_a) = \frac{1}{\alpha}\exp\left(\frac{j\pi\Delta x_m^2(v^2-2a)}{2a\lambda R_0}\right)\exp\left(\frac{j\pi v\Delta x_m}{a}\left(f_a+\frac{2v_r}{\lambda}\right)\right)\bar{H}(f_a) \tag{10}$$

where $\alpha = a/v^2$, and $\bar{H}(f_a)$ is the Fourier transform of $\bar{h}(t_m)$.

To achieve wide-swath imaging, the PRF employed by MIMO SAR systems is typically lower than the Doppler bandwidths of both stationary and maneuvering targets [16], which inevitably leads to azimuth aliasing. Consequently, (10) can be further expressed as:

$$H_m(f_b) = \frac{1}{\alpha}\sum_i \exp\left(\frac{j\pi\Delta x_m^2(v^2-2a)}{2a\lambda R_0}\right)\exp\left(\frac{j\pi v\Delta x_m}{a}\left(f_{bi}+\frac{2v_r}{\lambda}\right)\right)\bar{H}(f_{bi}) \tag{11}$$

where $f_{bi} = f_b + i\mathrm{PRF}$, $f_b \in [-\mathrm{PRF}/2, \mathrm{PRF}/2]$ and $i \in [-(M-1)/2, (M-1)/2]$.

The vector form of the azimuth received signal can be expressed as:

$$\boldsymbol{H}(f_b) = \frac{1}{\alpha}\boldsymbol{R}(f_b)\bar{\boldsymbol{H}}(f_b) \tag{12}$$

where

$$\boldsymbol{H}(f_b) = [H_1(f_b), H_2(f_b), \ldots, H_M(f_b)]^T \tag{13}$$

$$\boldsymbol{R}(f_b) = [\boldsymbol{r}_{i_{\min}}(f_b), \ldots, \boldsymbol{r}_{i_{\max}}(f_b)] \tag{14}$$

$$\boldsymbol{r}_i(f_b) = \left[\exp\left(\frac{j\pi\Delta x_1^2(v^2-2a)}{2a\lambda R_0}\right)\exp\left(\frac{j\pi v\Delta x_1}{a}\left(f_{bi}+\frac{2v_r}{\lambda}\right)\right), \ldots, \exp\left(\frac{j\pi\Delta x_M^2(v^2-2a)}{2a\lambda R_0}\right)\exp\left(\frac{j\pi v\Delta x_M}{a}\left(f_{bi}+\frac{2v_r}{\lambda}\right)\right)\right]^T \tag{15}$$

$$\bar{\boldsymbol{H}}(f_b) = \left[\bar{H}(f_b + i_{\min}\mathrm{PRF}), \ldots, \bar{H}(f_b + i_{\max}\mathrm{PRF})\right]^T \tag{16}$$

In the above equations, $i_{\min} = -(M-1)/2$, $i_{\max} = (M-1)/2$, and $[\cdot]^T$ denotes the matrix transpose. Building upon this formulation, $\alpha\boldsymbol{R}^{-1}(f_b)$ characterizes the reconstruction filter for maneuvering targets. The precise construction of this filter is premised on acquiring the target's radial velocity and radial acceleration. Once the accurate motion parameters are obtained and this reconstruction filter is derived, left-multiplying (12) by $\alpha\boldsymbol{R}^{-1}(f_b)$ can effectively resolve the aliasing caused by azimuth undersampling, thereby achieving an unambiguous reconstruction of the true Doppler spectrum. To address the challenge that characteristics of the maneuvering target are severely obscured by strong background clutter in practical detection scenarios, the next section of this paper focuses on how to estimate these two core maneuvering parameters in such a complex interferometric environment.

3. CLUTTER SUPPRESSION AND MANEUVERING TARGET PARAMETER ESTIMATION

The flowchart of the proposed algorithm is illustrated in Fig. 3, which consists of three main components: clutter suppression, radial acceleration estimation, and radial velocity estimation. These three parts are detailed below.

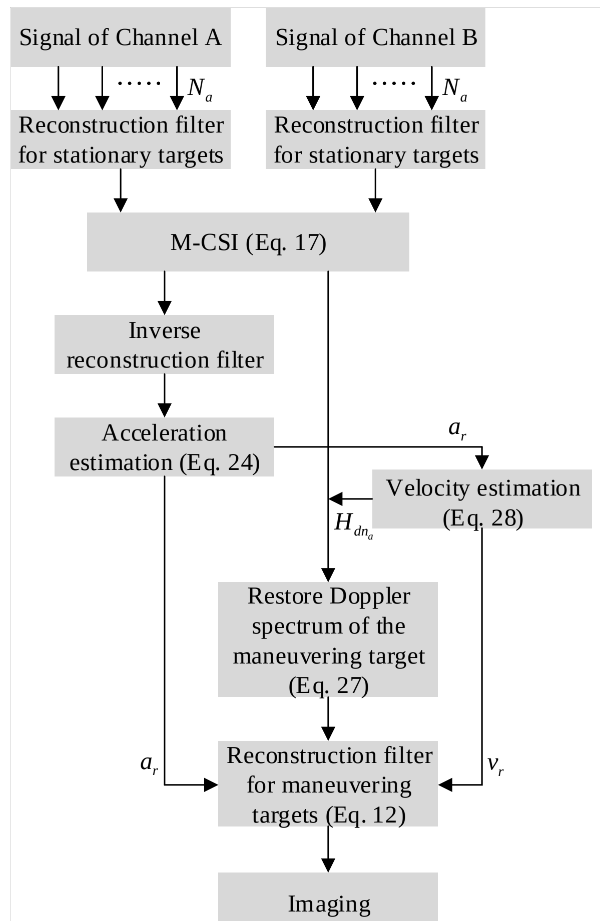

FIGURE 3. Flowchart of the proposed method.

3.1. Clutter Suppression for MIMO SAR

The prerequisite for extracting maneuvering target parameters is eliminating background interference from strong surface clutter. Considering that the conventional M-CSI cannot effectively accommodate the azimuth undersampling (low PRF) characteristics of spaceborne MIMO SAR, the M equivalent spatial receiving channels provided by the system are sequentially regrouped into two observation sub-arrays: equivalent Channel A, composed of the first N_a channels from waveform 1, and equivalent Channel B, composed of the last N_a channels from waveform 2. In the specific processing pipeline, signals of these two sub-arrays must first pass through the reconstruction filter for stationary targets [15] to complete the preprocessing for spectrum unaliasing and subsequently enter the dual-channel interferometric cancellation model. This joint mechanism can not only effectively suppress clutter components but also preserve the true signal energy of the maneuvering target losslessly to the maximal extent.

Based on the geometric relationship shown in Fig. 1, since the two orthogonal waveforms are transmitted synchronously, the relative time delay of their echo signals at the receiver primarily depends on the one-way propagation stage from the transmitter to the illuminated target. Under the assumption that the far-field condition is satisfied (i.e., the red and blue rays representing the transmitted waveforms in Fig. 1 can be regarded as parallel), the spatial path difference generated between Channel A and Channel B can be approximately expressed as $(N_a-1)d_a\sin\theta$. Consequently, the interferometric phase difference between the two equivalent channels derived from this is $\phi_c=-2\pi(N_a-1)d_a\sin\theta/\lambda$.

Let $z_A(l,k)$ and $z_B(l,k)$ denote complex signals of the corresponding pixels in the images acquired by the two equivalent receiving channels, respectively, where l and k represent indices of the range and azimuth bins, respectively. Utilizing the interferometric phase difference between the two equivalent channels to perform pixel-by-pixel compensation on the image of Channel B, and subsequently subtracting the compensated images of the two channels yields:

$$z_{out}(l,k)=z_A(l,k)\exp\left(\frac{j\phi_c}{2}\right)-z_B(l,k)\exp\left(\frac{-j\phi_c}{2}\right) \tag{17}$$

Ideally, the components obtained at this stage contain only maneuvering target information, and the residual maneuvering signal can be expressed as:

$$z_{out}(l,k)=s_A(l,k)\exp\left(\frac{j\phi_c}{2}\right)-s_B(l,k)\exp\left(\frac{-j\phi_c}{2}\right) \tag{18}$$

where $s_A(l,k)$ and $s_B(l,k)$ denote the maneuvering target signals in Channels and B, respectively. They satisfy the following relationship: $s_B(l,k)=s_A(l,k)e^{j\phi_t}$, where ϕ_t represents the interferometric phase difference of the maneuvering target signal between the two channels. Therefore, (18) can be further expressed as:

$$z_{out}(l,k)=s_A(l,k)\exp\left(\frac{j\phi_t}{2}\right)\left(2j\sin\frac{\phi_c-\phi_t}{2}\right) \tag{19}$$

Through the aforementioned operations, the system can effectively suppress ground clutter, thereby significantly improving the signal-to-clutter ratio (SCR) of the observed region. This processing not only allows the weak energy of the maneuvering target, originally deeply buried in the clutter environment, to emerge clearly, but also fundamentally eliminates the severe corruption of the Doppler spectrum distribution caused by background residuals. Consequently, it establishes a vital data foundation and prerequisite for the subsequent estimation of radial acceleration a_r and radial velocity v_r.

3.2. Radial Acceleration Estimation of Maneuvering Target

After clutter suppression, obscured maneuvering target signals emerge. By passing maneuvering target signals through the inverse reconstruction filter for stationary targets [15], maneuvering target signals can be obtained as:

$$\begin{aligned} s_{n_a}(t_m)=&\exp\left(\frac{-j4\pi R_0}{\lambda}\right)\exp\left(\frac{-j\pi\Delta x_{n_a}^2}{\lambda R_0}\right)\\ &\exp\left(\frac{-j2\pi(2v_rR_0+v\Delta x_{n_a})}{\lambda R_0}t_m\right)\\ &\exp\left(\frac{-j2\pi(a_rR_0+v^2)}{\lambda R_0}t_m^2\right)\exp\left(j\frac{\phi_t}{2}\right)\end{aligned} \tag{20}$$

where ϕ_t can be regarded as constant over the entire synthetic aperture time. For convenience of subsequent discussion, let $v_q=\frac{2v_rR_0+v\Delta x_{n_a}}{\lambda R_0}$, $K_q=\frac{a_rR_0+v^2}{\lambda R_0}$, and $g(t_m)=\exp\left(\frac{-j4\pi R_0}{\lambda}\right)\exp\left(\frac{-j\pi\Delta x_{n_a}^2}{\lambda R_0}\right)\exp\left(j\frac{\phi_t}{2}\right)$, then (20) can be expressed as:

$$s_{n_a}(t_m)=g(t_m)\exp(-j2\pi v_qt_m)\exp(-j2\pi K_qt_m^2) \tag{21}$$

where $t_m\in(-T_a/2,T_a/2)$.

Dividing $s_{n_a}(t_m)$ into two sub-apertures, each spanning a duration of $T_a/2$ can be expressed as:

$$\begin{aligned} s_{n_a}^{early}(t_m)=&\,g\left(t_m-\frac{T_a}{4}\right)\exp\left(-j2\pi v_q\left(t_m-\frac{T_a}{4}\right)\right)\\ &\exp\left(-j2\pi K_q\left(t_m-\frac{T_a}{4}\right)^2\right)\\ =&\left[g\left(t_m-\frac{T_a}{4}\right)\exp(-j2\pi v_qt_m)\right.\\ &\left.\exp\left(-j2\pi K_q\left(t_m^2+\frac{T_a^2}{16}\right)\right)\right]\\ &\exp\left(j2\pi v_q\frac{T_a}{4}\right)\exp\left(j2\pi\frac{K_qT_a}{2}t_m\right)\end{aligned} \tag{22}$$

$$\begin{aligned} s_{n_a}^{late}(t_m)=&\,g\left(t_m+\frac{T_a}{4}\right)\exp\left(-j2\pi v_q\left(t_m+\frac{T_a}{4}\right)\right)\\ &\exp\left(-j2\pi K_q\left(t_m+\frac{T_a}{4}\right)^2\right)\\ =&\left[g\left(t_m+\frac{T_a}{4}\right)\exp(-j2\pi v_qt_m)\right.\\ &\left.\exp\left(-j2\pi K_q\left(t_m^2+\frac{T_a^2}{16}\right)\right)\right]\\ &\exp\left(-j2\pi v_q\frac{T_a}{4}\right)\exp\left(-j2\pi\frac{K_qT_a}{2}t_m\right)\end{aligned} \tag{23}$$

where $t_m \in (-T_a/4, T_a/4)$. $g(t_m)$ and $\exp(j2\pi v_q T_a/4)$ are both constant terms, which have no impact on the frequency shift of the Fourier transforms of $s_{n_a}^{early}(t_m)$ and $s_{n_a}^{late}(t_m)$.

The relationship between the early and late sub-aperture signals in the frequency domain is given by:

$$S_{n_a}^{early}(f) = S_{n_a}^{late}(f - K_q T_a) \tag{24}$$

By performing cross-correlation on $S_{n_a}^{early}(f)$ and $S_{n_a}^{late}(f)$, a discrete correlation peak is initially detected. To overcome the limitation of grid quantization errors, a parabolic sub-pixel interpolation method [17] is subsequently applied to extract the highly precise lag amount $K_q T_a$ of $S_{n_a}^{early}(f)$ relative to $S_{n_a}^{late}(f)$. Based on this signal's time-frequency evolution characteristic, the target's radial acceleration parameter can be effectively and accurately inverted. The prior information of the radial acceleration not only fundamentally eliminates the unknown broadening effect in the Doppler frequency domain, but also establishes a crucial data foundation for subsequent estimation of the radial velocity and the systematic synthesis of the reconstruction filter for maneuvering targets.

3.3. Radial Velocity Estimation of Maneuvering Target

Following clutter suppression processing, introducing the interferometric phase alters the original signal structures of Channels A and B, rendering direct extraction of the original maneuvering target echoes from both channels extremely difficult. To this end, this section details how to use the reconstruction filter for stationary targets to restore the effective maneuvering target signal of Channel A from the canceled data, based on which the target radial velocity is subsequently estimated.

In previous related research [15], to counter the spectrum aliasing induced by low PRF undersampling in the azimuth direction, the mathematical process of resolving Doppler ambiguity and achieving spectrum reconstruction relying on the reconstruction filter for stationary targets can be characterized as:

$$\begin{bmatrix} Q_{11} & \dots & Q_{1N_a} \\ \vdots & \ddots & \vdots \\ Q_{N_a1} & \dots & Q_{N_aN_a} \end{bmatrix} \begin{bmatrix} H_1^{all} \\ \vdots \\ H_{N_a}^{all} \end{bmatrix} = I_A \tag{25}$$

where the coefficient matrix on the left represents the reconstruction filter for stationary targets. This reconstruction process is equivalent to sequentially applying N_a independent linear filtering components Q_{n_a} to the undersampled data captured by each receiving channel, and subsequently performing coherent accumulation on the outputs. Furthermore, a single reconstruction filter Q_{n_a} is essentially a filter bank jointly composed of N_a sub-bandpass filters $Q_{n_a n_a}$. The variable H^{all} characterizes the total echo signal, which contains a mixture of environmental clutter and maneuvering-target echoes. Meanwhile, I_A denotes the output spectrum component mapped through the aforementioned system. It should be emphasized that since the reconstruction filter for stationary targets is used to process all echo signals at this stage, the maneuvering-target signal component in I_A is not an ideal unambiguous spectrum.

Combining (17) and (25) yields (26).

$$\begin{bmatrix} Q_{11} & \dots & Q_{1N_a} & -Q_{11}\exp(-\phi_{c1}) & \dots & -Q_{1N_a}\exp(-\phi_{c1}) \\ \vdots & \ddots & \vdots & \vdots & \ddots & \vdots \\ Q_{N_a1} & \dots & Q_{N_aN_a} & -Q_{N_a1}\exp(-\phi_{cN_a}) & \dots & -Q_{N_aN_a}\exp(-\phi_{cN_a}) \end{bmatrix} \begin{bmatrix} H_1 \\ \vdots \\ H_{2N_a} \end{bmatrix} = I_{out} \tag{26}$$

$$\begin{bmatrix} Q_{11}(1 - H_{d1}\exp(-\phi_{c1})) & \dots & Q_{1N_a}(1 - H_{dN_a}\exp(-\phi_{c1})) \\ \vdots & \ddots & \vdots \\ Q_{N_a1}(1 - H_{d1}\exp(-\phi_{cN_a})) & \dots & Q_{N_aN_a}(1 - H_{dN_a}\exp(-\phi_{cN_a})) \end{bmatrix} \begin{bmatrix} H_1 \\ \vdots \\ H_{N_a} \end{bmatrix} = I_{out} \tag{27}$$

Given that the coefficient matrix in (26) is rank-deficient, a unique analytical solution (i.e., $H_1, \dots, H_{2N_a}$) cannot be directly obtained; thus, additional constraint equations must be introduced to achieve the precise reconstruction of the maneuvering target's original spectrum. In-depth analysis reveals that the profile of the observed spectrum H_m not only undergoes a frequency-domain shift due to the radial velocity v_r, but is also modulated by the radial acceleration a_r, leading to severe spectral broadening. Furthermore, this frequency-domain response is tightly coupled with the target's inherent scattering signal intensity.

To overcome the predicament of the aforementioned parameter coupling, a ratio factor $H_{dn_a} = H_{n_a+N_a}/H_{n_a}$ resistant to amplitude interference is constructed. Since the echo amplitudes of the same physical target remain consistent across all equivalent azimuth channels, this ratio factor successfully eliminates the influence of signal intensity, and its value is jointly determined solely by the target's instantaneous slant range, radial velocity, and radial acceleration. Considering that the target slant range can be directly extracted from the residual data after clutter suppression and that the radial acceleration has already been estimated in the previous stage, obtaining H_{dn_a} subsequently only requires a traversal search over the target radial velocity. Substituting it into (26) yields (27).

The coefficient matrix in (27) satisfies full-rank property, thereby allowing the unique analytical solution for the maneuvering target signal in Channel A (i.e.,$H_1, \dots, H_{N_a}$) to be directly obtained. On this basis, relying on the currently traversed radial velocity parameter and the previously obtained radial acceleration estimate, a matching reconstruction filter for maneuvering targets is constructed. Subsequently, the preliminarily inverted maneuvering target signal is passed through this filter and subjected to pulse compression. To achieve the optimal estimation of parameters, an evaluation criterion based on the signal energy concentration after pulse compression is con-

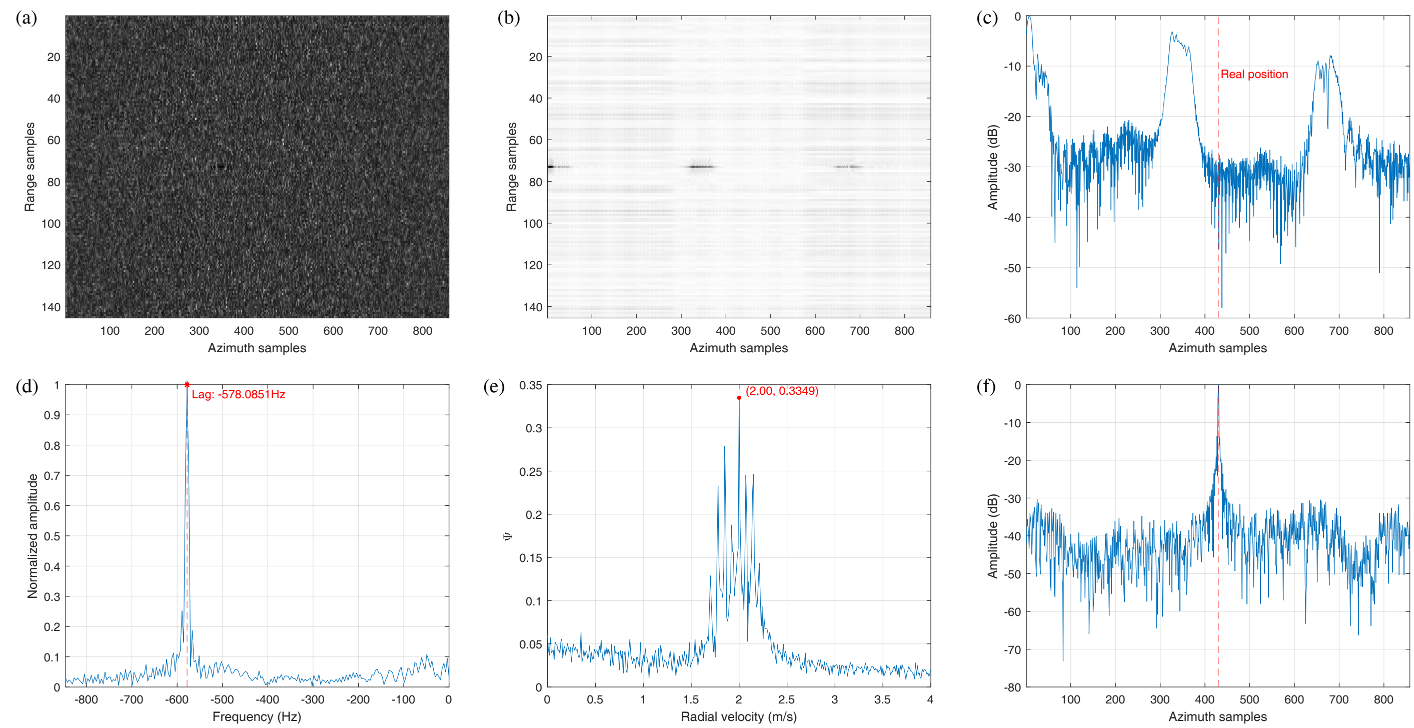

FIGURE 4. Results of the proposed method at an SCR of 13 dB. (a) Imaging result of the scene containing clutter, (b) clutter suppression result, (c) profile plot of the clutter suppression result, (d) sub-aperture frequency offset, (e) radial velocity estimation result, and (f) final focused imaging result.

structed, which can be mathematically expressed as:

$$\Psi = \frac{\int E(\hat{v}_r)\mathrm{rect}[t_m/T]dt_m}{\int E(\hat{v}_r)dt_m} \tag{28}$$

where $E(\hat{v}_r)$ denotes the azimuth accumulated signal energy after pulse compression, and $\mathrm{rect}[t_m/T]$ represents a window function with a span of T. Leveraging this optimization mechanism, the algorithm identifies the global peak of energy concentration and selects its corresponding radial velocity v_r and original spectrum (i.e., $H_1, \ldots, H_{N_a}$) as the optimal output. Then, the original spectrum is passed through the reconstruction filter for maneuvering targets, which is designed based on the estimated radial acceleration and radial velocity, to obtain an unambiguous spectrum of the target. Subsequently, high-precision focused imaging is achieved via pulse compression.

Upon completion of the focused imaging procedure, we analyze the azimuth computational complexity of the proposed framework. Let K, L, and N denote the number of azimuth samples and search grids for radial acceleration and radial velocity, respectively, with the number of complex multiplications and additions used as the metric and lower-order terms ignored. The conventional GRFT relies on a two-dimensional traversal search, resulting in a complexity of $\mathcal{O}(LNK)$. In contrast, our proposed method decouples the estimation process: radial acceleration is solved analytically via fast Fourier transforms (FFTs) with $\mathcal{O}(K \log K)$ complexity, leaving only a one-dimensional search for velocity requiring $\mathcal{O}(NK \log K)$. Consequently, the overall complexity is significantly reduced to $\mathcal{O}(NK \log K)$. Since $L \gg \log K$ in practice, the proposed algorithm successfully avoids the prohibitive multi-dimensional computational burden.

4. SIMULATION RESULTS AND ANALYSIS

To verify the effectiveness of the proposed method, simulated data are processed using the system parameters listed in Table 1. To approximate a realistic scenario, stationary point targets are distributed within the imaging scene, and their radar cross sections (RCS) are set to random values with a variance of 1. Additionally, a maneuvering target with a radial velocity of 2 m/s and a radial acceleration of 2.5 m/s^2 is positioned at the center of the scene.

TABLE 1. Parameters of the MIMO SAR system.

Parameters	Values
Central carrier frequency	5.3 GHz
Platform velocity	7100 m/s
The nearest slant range	850 km
Signal bandwidth	25 MHz
Pulse width	10 µs
PRF	850 Hz
Length of the azimuth antennas	4.8 m
Adjacent subchannel spacing	1.6 m
Number of transmitting channels	2
Number of receiving subchannels in azimuth	3
Doppler bandwidth	1350 Hz

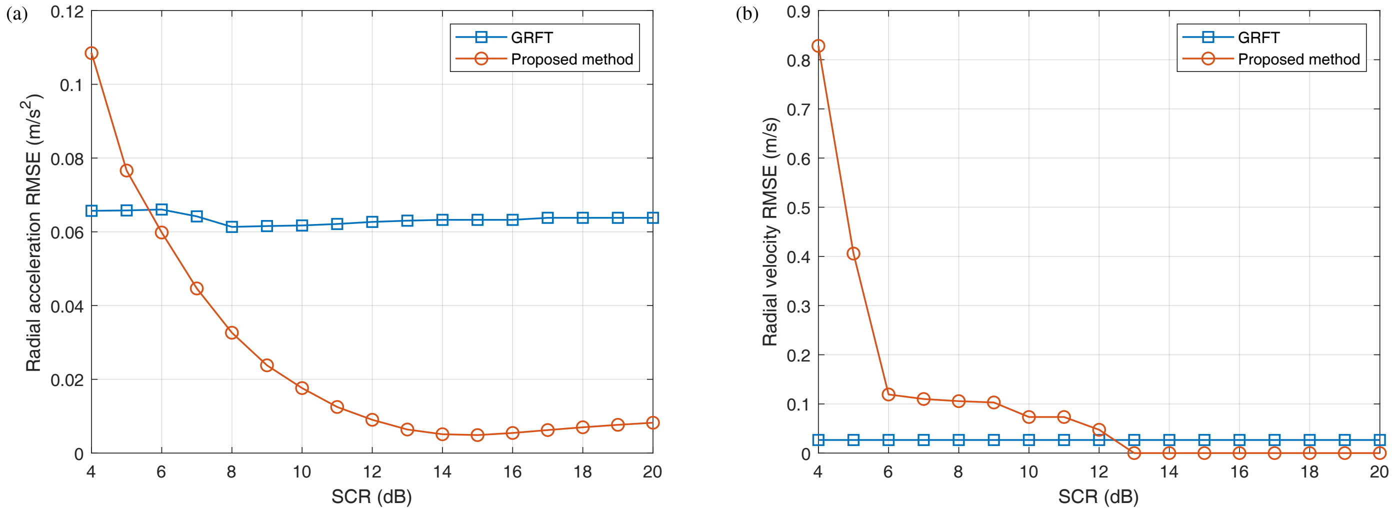

FIGURE 5. Performance verification and comparison of the proposed method. (a) Radial acceleration error versus SCR and (b) Radial velocity error versus SCR.

Figure 4 illustrates the simulation results at an SCR of 13 dB. Fig. 4(a) shows the imaging result of the Channel A signal after passing through the reconstruction filter for stationary targets when the SCR is 13 dB. The scene contains clutter and a moving target, where the moving target signal is completely submerged in the clutter. Fig. 4(b) illustrates the clutter suppression result. The clutter is effectively suppressed. Although the moving target information is preserved in the image, its imaged position is incorrect, and artifacts induced by the mismatched reconstruction filter, along with defocusing caused by the acceleration, are present. Fig. 4(c) shows the profile plot of the clutter suppression effect within the imaging range; it can be observed that the maneuvering target is imaged at an incorrect position, accompanied by defocusing and artifact problems. Subsequently, the maneuvering target signal is extracted from the clutter-suppressed components, passed through the inverse reconstruction filter for stationary targets, and then subjected to radial acceleration estimation. The frequency offset between the two sub-apertures is displayed in Fig. 4(d), which indicates that $S_{n_a}^{early}(f)$ lags behind $S_{n_a}^{late}(f)$ by 578.0851 Hz. Based on this value, the acceleration is calculated to be 2.50196 m/s^2, which differs from the actual value of the maneuvering target by only 0.00196 m/s^2. Then, the estimated radial acceleration is fed into the radial-velocity estimation algorithm combined with the reconstruction filter for stationary targets. This algorithm accurately estimates the moving target's radial velocity of 2 m/s, and this result is demonstrated in Fig. 4(e). Finally, a reconstruction filter for maneuvering targets is designed using the estimated radial acceleration and radial velocity, and pulse-compression imaging is performed to yield Fig. 4(f). By comparing Fig. 4(c) with Fig. 4(f), it is revealed that due to the accurate velocity estimation, the target can be accurately imaged; moreover, owing to the designed reconstruction filter for maneuvering targets, artifacts are eliminated, and the defocusing problem is resolved. The energy concentration after pulse compression in Fig. 4(f) is relatively degraded. This is attributed to that under low-SCR conditions, system channel errors limit the M-CSI-based clutter suppression performance, resulting in residual clutter in I_{out}. Furthermore, the slight estimation error in radial acceleration reduces the matching degree between the maneuvering target signal and the ratio factor, ultimately leading to degrading energy concentration.

To evaluate the robustness of the proposed method, 50 independent Monte Carlo trials are conducted under different clutter realizations while holding the motion parameters of the maneuvering target constant (specifically, a radial velocity of 2 m/s and a radial acceleration of 2.5 m/s^2). The SCR of the echo signals ranges from 4 dB to 20 dB with an increment of 1 dB. Root-mean-square error (RMSE) is adopted to measure the error performance of radial acceleration and radial velocity estimation. The GRFT algorithm is selected as the baseline. Both algorithms perform parameter estimation after applying the clutter suppression method proposed in this paper. For both algorithms, the radial-velocity search range spans from 0 to 4 m/s with a step size of 0.01 m/s. Furthermore, the radial acceleration search range for the GRFT algorithm is set from 0 to 4 m/s^2 with a step size of 0.01 m/s^2.

Figure 5 presents the performance verification and comparison of the proposed method. Fig. 5(a) illustrates the variation trends of radial acceleration estimation errors for both algorithms with respect to the SCR. It can be observed that the error of the GRFT algorithm remains essentially constant at 0.06 m/s^2 across the entire SCR range, which is constrained by the algorithm's inherent limitations. In contrast, the error of the proposed method continuously decreases as the SCR increases. At 6 dB, its error falls below that of the GRFT for the first time and continues to decline thereafter, maintaining a minimum error of approximately 0.01 m/s^2. This demonstrates that the proposed radial acceleration estimation algorithm outperforms the GRFT in terms of estimation accuracy. Furthermore, while the GRFT algorithm requires a computationally expensive traversal search among candidate values, the proposed acceleration estimation method is completely search-free. Fig. 5(b) presents radial velocity estimation errors of the two algorithms. Simi-

TABLE 2. Comparison of computational efficiency.

Algorithm	Number of Search Points	Average Time Per Trial (s)	Total Simulation Time (s)
GRFT	401×401	195.488	9774.400
Proposed	401	29.301	1465.050

larly restricted by inherent algorithmic limitations, the radial-velocity estimation error of the GRFT algorithm stabilizes at approximately 0.02 m/s. For the proposed method, the estimation error gradually decreases as the SCR increases. Notably, the RMSE curve drops sharply around 5 dB; as the SCR rises to 6 dB, the error is slightly above 0.1 m/s, which approaches the performance of the GRFT algorithm. Thereafter, the decline becomes more gradual, ultimately reaching and maintaining its minimum value at 13 dB, which remains lower than the error of the GRFT.

Under low-SCR conditions, the initial clutter suppression step inevitably leaves a relatively large amount of residual clutter. Unlike the GRFT baseline, which leverages a two-dimensional global coherent integration to maximize processing gain and naturally suppress random residuals, the proposed method is inherently limited by its cascaded architecture and algebraic reconstruction mechanism. First, the parameter estimation is sequential; thus, any slight deviation in the initial radial acceleration estimate due to strong clutter directly propagates into the subsequent radial velocity search. Second, the algorithm reconstructs the original spectrum by solving a system of linear equations parameterized by the ratio factor. In this linear system, residual clutter acts as a significant perturbation in the observation vector. During matrix inversion and reconstruction, this structured noise is inherently amplified, severely degrading the matching degree and distorting the recovered target spectrum. Finally, the optimal velocity is determined by evaluating the energy concentration within a temporal window after pulse compression. Under severe clutter interference, a mismatched velocity candidate may inadvertently smear the residual noise, causing a high accumulation of spurious energy within the window. This results in a deceptively high metric score without forming a sharply focused, sinc-like mainlobe, ultimately misleading the peak search and causing larger estimation errors. Once the initial SCR improves and the residual clutter is sufficiently small, the error propagation is mitigated, the linear reconstruction stabilizes, and the proposed algorithm achieves highly accurate radial velocity estimation.

Finally, the computational efficiency is evaluated by analyzing the execution time required for simulation experiments. All experiments were performed on a computing platform equipped with an Intel Core i7-10510U CPU @ 1.80 GHz and 8 GB RAM, using MATLAB R2023b. The detailed execution times are listed in Table 2. To achieve high estimation accuracy, the conventional GRFT requires a dense 2-D joint grid search (401×401) over the acceleration and velocity parameter space. In contrast, the proposed algorithm uses only 401 search points for velocity estimation due to its inherently decoupled parameter estimation structure. Consequently, the average execution time per trial is drastically reduced from 195.488 s to 29.301 s. This represents an approximately 6.7-fold improvement in computational efficiency, reducing the total simulation time for the 50 Monte Carlo trials from about 2.72 hours to merely 0.41 hours.

5. CONCLUSION

In this paper, aiming at the challenges of strong clutter interference and unknown motion parameters faced by spaceborne MIMO SAR systems when observing a ground maneuvering target, a comprehensive method integrating clutter suppression, maneuvering parameter estimation, and focused imaging is proposed. First, the signal model incorporating target radial velocity and radial acceleration is refined, and the corresponding reconstruction filter for maneuvering targets is derived. Second, the effective suppression of static background clutter is achieved by utilizing the extended M-CSI algorithm. On this basis, the radial acceleration deeply buried in the residual signals is accurately extracted via inverse reconstruction filtering and sub-aperture frequency-domain cross-correlation techniques. Subsequently, a ratio factor resistant to amplitude interference is constructed to achieve precise estimation of the radial velocity. Simulation results quantitatively validate the superiority and robustness of the proposed method. Specifically, the proposed search-free radial acceleration estimation achieves a minimum RMSE of approximately 0.01 m/s^2, outperforming the 0.06 m/s^2 limit of the GRFT baseline. Furthermore, the radial velocity estimation error continuously decreases with an increasing SCR, ultimately dropping below the GRFT's 0.02 m/s error bound at an SCR of 13 dB. In single-trial validations at an SCR of 13 dB, the absolute estimation error for acceleration was as low as 0.00196 m/s^2. Consequently, the proposed method thoroughly eliminates defocusing and image artifact phenomena induced by radial acceleration, demonstrating highly precise and favorable imaging performance. Despite these advantages, the proposed cascaded architecture and algebraic reconstruction mechanism exhibit sensitivity in extreme low-SCR environments. Specifically, severe residual clutter can cause sequential error propagation, amplify structured noise during linear matrix inversion, and mislead the energy-concentration-based selection metric. Therefore, future work will focus on enhancing algorithmic robustness under such challenging conditions. Potential methodological improvements include integrating advanced sparse decomposition techniques for superior initial clutter-target separation, developing joint-optimization frameworks to mitigate cascaded error propagation, and introducing mainlobe-shape-constrained evaluation metrics (e.g., image contrast or entropy) to prevent spurious energy accumulation during velocity selection. Furthermore, the current study is established on the assumption of ideal waveform separation. In practical spaceborne MIMO SAR systems, imperfect echo separation can introduce residual interference and estimation bias. Therefore, comprehensively analyzing the influence of echo separation errors and developing robust parameter estimation strategies under non-ideal separation conditions will be a critical focus of our future research.

REFERENCES

[1] Moreira, A., P. Prats-Iraola, M. Younis, G. Krieger, I. Hajnsek, and K. P. Papathanassiou, "A tutorial on synthetic aperture radar," *IEEE Geoscience and Remote Sensing Magazine*, Vol. 1, No. 1, 6–43, 2013.

[2] Gebert, N., G. Krieger, and A. Moreira, "Digital beamforming on receive: Techniques and optimization strategies for high-resolution wide-swath SAR imaging," *IEEE Transactions on Aerospace and Electronic Systems*, Vol. 45, No. 2, 564–592, 2009.

[3] Wang, L.-B., D.-W. Wang, J.-J. Li, J. Xu, C. Xie, and L. Wang, "Ground moving target detection and imaging using a virtual multichannel scheme in HRWS mode," *IEEE Transactions on Geoscience and Remote Sensing*, Vol. 54, No. 9, 5028–5043, 2016.

[4] Zhang, Y., Y. Deng, Z. Zhang, W. Wang, T. Wei, and R. Wang, "A two-stage echo separation scheme for spaceborne MIMO-HWRS SAR system," *IEEE Transactions on Geoscience and Remote Sensing*, Vol. 60, 1–14, 2022.

[5] Krieger, G., "MIMO-SAR: Opportunities and pitfalls," *IEEE Transactions on Geoscience and Remote Sensing*, Vol. 52, No. 5, 2628–2645, 2014.

[6] Wang, Y., G. Jin, T. Shi, H. Yan, A. Jakobsson, X. Wang, S. Niu, H. Zhang, X. Zhang, D. Wu, and D. Zhu, "A novel MIMO-SAR echo separation solution for reducing the system complexity: Spectrum preprocessing and segment synthesis," *IEEE Transactions on Geoscience and Remote Sensing*, Vol. 61, 1–17, 2023.

[7] Zhang, H., G. Jin, H. Zhang, Y. Wang, Y. Cheng, Z. Guo, S. Ye, and D. Zhu, "A fast repeater mainlobe deceptive jamming suppression method for FDA-MIMO SAR under complex motion condition," *IEEE Transactions on Aerospace and Electronic Systems*, Vol. 62, 862–878, 2026.

[8] Wacks, S. and B. Yazıcı, "Doppler-DPCA and Doppler-ATI: Novel SAR modalities for imaging of moving targets using ultra-narrowband waveforms," *IEEE Transactions on Computational Imaging*, Vol. 4, No. 1, 125–136, 2018.

[9] El Khatib, A., K. Assaleh, and H. Mir, "Space-time adaptive processing using pattern classification," *IEEE Transactions on Signal Processing*, Vol. 63, No. 3, 766–779, 2015.

[10] Li, Z., Y. Zhang, H. Liu, and Y. Guo, "Training samples selection method for space-time adaptive processing based on clutter covariance matrix reconstruction," *Electronics Letters*, Vol. 53, No. 14, 953–954, 2017.

[11] Li, Y., M. Shen, L. Qiao, D. Wu, and D. Zhu, "Ground moving target imaging for spaceborne MIMO SAR using reconstruction filter priors," *IEEE Geoscience and Remote Sensing Letters*, Vol. 23, 4 007 705–4 007 705, 2026.

[12] Xu, J., X.-G. Xia, S.-B. Peng, J. Yu, Y.-N. Peng, and L.-C. Qian, "Radar maneuvering target motion estimation based on generalized Radon-Fourier transform," *IEEE Transactions on Signal Processing*, Vol. 60, No. 12, 6190–6201, 2012.

[13] Xu, J., J. Yu, Y.-N. Peng, and X.-G. Xia, "Radon-Fourier transform for radar target detection, I: Generalized Doppler filter bank," *IEEE Transactions on Aerospace and Electronic Systems*, Vol. 47, No. 2, 1186–1202, 2011.

[14] Qiao, L., M. Shen, G. Jin, D. Wu, and D. Zhu, "An efficient motion parameters estimation method for ground maneuvering targets in wide-swath MIMO-SAR," *IEEE Journal of Selected Topics in Applied Earth Observations and Remote Sensing*, Vol. 19, 14 723–14 736, 2026.

[15] Krieger, G., N. Gebert, and A. Moreira, "Unambiguous SAR signal reconstruction from nonuniform displaced phase center sampling," *IEEE Geoscience and Remote Sensing Letters*, Vol. 1, No. 4, 260–264, 2004.

[16] Zhang, Z., W. Yu, M. Zheng, L. Zhao, and Z.-X. Zhou, "Robust clutter suppression and radial velocity estimation for high-resolution wide-swath SAR-GMTI," *Remote Sensing*, Vol. 14, No. 7, 1555, 2022.

[17] Pallotta, L., G. Giunta, and C. Clemente, "Subpixel SAR image registration through parabolic interpolation of the 2-D cross correlation," *IEEE Transactions on Geoscience and Remote Sensing*, Vol. 58, No. 6, 4132–4144, 2020.